Predictions of polymer migration in a dilute solution between rotating eccentric cylinders

Junting Xiang[1], Elnaz Hajizadeh[1], Ronald Larson[2], Damian Nelson[1]*

[1]Department of Mechanical Engineering, The Faculty of Engineering and Information Technology, University of Melbourne, Parkville, VIC 3010, Australia

[2]Department of Chemical Engineering, University of Michigan, Ann Arbor, MI 48109, USA

[*]Corresponding author: ellie.hajizadeh@unimelb.edu.au

Abstract

Our recent continuum theory for stress-gradient-induced migration of polymers in confined solutions, including the depletion from the solid boundaries (*E. Hajizadeh* and *R. G. Larson*, *Soft Matter*, 2017, **13**, 5942) [1] is applied to a two-dimensional rotational shearing flow in the gap between eccentric cylinders. Analytical results for the steady-state distribution of polymer dumbbells in the limit of dilute polymer solution $c/c* \ll 1$ ($c*$ is the chain overlap concentration) and in the absence of hydrodynamic interactions (HI) are obtained. The effects of eccentricity e, and of three perturbation variables, namely Weissenberg number Wi, Gradient number Gd (which defines the level of polymer chain confinement) and Peclet number Pe on the polymer concentration pattern are investigated. The stress-gradient-induced migration results in polymer migration towards the inner cylinder, while wall-depletion-induced migration results in near-zero polymer concentration close to flow boundaries, which couples to a stress-gradient-induced migration effect. In the presence of wall-depletion, we obtain first order concentration variation proportional to Wi. Whereas, in the absence of wall-depletion, there is no first order contribution and therefore lowest-order concentration variation is proportional to Wi^2. An upper limit of Wi = 1.6 exists, beyond which numerical solution demands an excessive under-relaxation to converge. In addition, for a high degree of polymer chain confinement, i.e., for Gd greater than 0.5, the continuum theory fails to be accurate and mesoscopic simulations that track individual polymer molecules are needed.

1. Introduction

The cross-streamline migration of polymers in solution in confined flows with steep changes in stress or velocity gradient is a well-known phenomenon that leads to a nonuniform polymer concentration profile within the flow domain. Apart from its scientific importance [2], the phenomenon has implications for several technological applications in lubrication [3, 4], enhanced oil recovery [5], separation processes [6, 7], and DNA sequencing in microfluidics [8, 9]. For instance, predicting the conformation and motion of polymer chains in microfluidic geometries is of considerable significance in designing efficient devices for single-molecule analysis of DNA [10-14]. While simple spherical colloids in confined geometries usually migrate from regions of high to low shear rates due to direct interactions between the colloids, with a corresponding transport coefficient proportional to the shear-rate derivative of the pair-correlation function [15, 16], migrations of non-interacting polymers can be more complicated due to the coupling of the polymer conformation tensor to the second derivative of the velocity field [1].

Theories for polymer migration typically involve incorporating into the mass balance equation a polymer ‘‘stress-diffusion’’ term, proportional to the divergence of the polymer stress tensor, which can be derived in a variety of ways, such as by using the two-fluid model [4, 7, 17-21]. Other approaches, including perturbation expansions within the phase space kinetic theory [4, 17] and ‘‘body tensor continuum theory’’ proposed by Öttinger [22] all result in mass transport terms that include the divergence of the stress tensor, and other terms that appear in both the polymer mass balance equation and the polymer constitutive equation and that differ among the various approaches mentioned above [17].

We have recently developed a continuum theory [23] for the stress-gradient-induced migration of polymers in solutions based on a systematic perturbation analysis and validated, for the first time, through mesoscopic bead-spring simulations, which successfully identifies the migration source and clarifies the origin of discrepancies among the existing theories. The work shows that some terms arising in existing theories are due to the inclusion of higher order terms in an expansion in a perturbation parameter Gd, which is a measure of the degree of polymer chain confinement. Specifically, Gd is the ratio of polymer radius of gyration to the length scale over which a steep change in velocity gradient occurs, as discussed in section 3. We earlier demonstrated that in dilute

solutions migration arises from the second and higher order spatial gradients in velocity. This continuum theory has been applied to a periodic vortex flow [23], periodic electroosmotic flow [9], and concentric cylinder flow [1]. In the latter, we observed a strong polymer migration towards the inner cylinder and confirmed this phenomenon and the range of accuracy of the continuum theory via Brownian dynamics [24] simulations [1].

Here, we wish to extend our recent continuum theory to the flow in the gap between *eccentric* cylinders, which is an important model problem for journal bearing flows. In practical applications, such flows often involve lubricants that contain polymer additives, whose migration would be a significant concern, making this problem a potentially important one for lubricant design and tribology.

In this paper, we follow our previous work and use the simple Hookean dumbbell model for polymer chains in a dilute solution flowing in the gap between rotating eccentric cylinders. We first examine the effect of dimensionless numbers Gradient number Gd, Weissenberg number Wi, and Peclet number Pe on polymer migration pattern to determine the range of validity of the continuum theory. Thereafter, we study the effect of wall-depletion on migration patterns, using a wall repulsion potential given by a decaying-exponential potential fitted to results from our previous Brownian dynamics simulations [1]. This empirical wall potential was shown, by comparison to predictions of bead-spring simulations, to account well for the wall-depletion effect for concentric Taylor Couette flow. Since we have not changed the polymer chain model or the wall parameters, this model is also used in the present study for the case of eccentric cylinders. In what follows, Section 2 describes the eccentric cylinder geometry and flow field; Section 3 defines the dimensionless groups used in our analyses; Section 4 presents the details of the perturbation theory for polymer dumbbells in cylindrical coordinates; Section 5 discusses the results for the stress-gradient-induced migration and depletion-induced migration; and ultimately, Section 6 summarises the main findings and future work.

2. Geometry and Flow Field

For our eccentric cylinders, depicted in Figure 1, the inner cylinder rotates counter-clockwise while the outer cylinder remains stationary, producing shear flow between them. R_1 and R_2 are the radii

of the inner and outer cylinders, e is the eccentricity which is the offset between the centres of the two cylinders, Ω is the angular velocity of inner cylinder, and x and y are local Cartesian coordinates to assist analysing flow in the gap between the two cylinders.

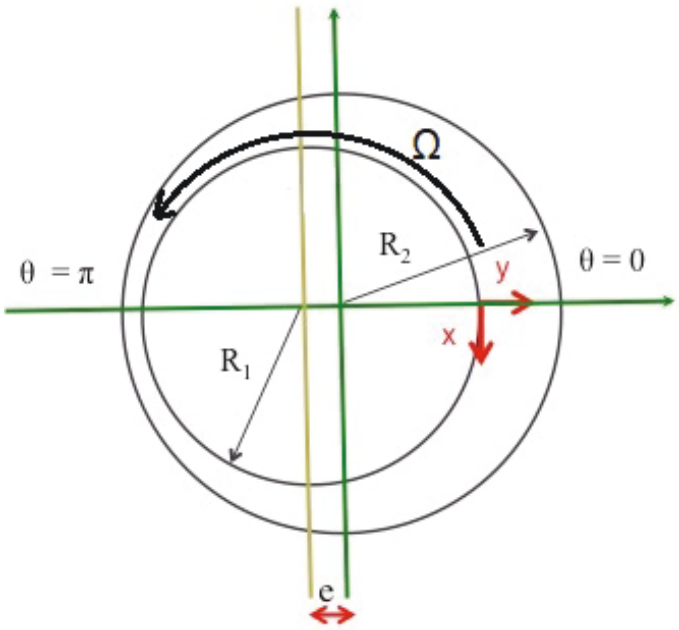

Figure 1 Schematic representation of the eccentric cylinder system

It has been shown [25] that for a slow laminar flow in a small gap between the eccentric cylinders relative to the cylinder's radius, the velocity components using a lubrication approximation are given by

$$V_\theta(r,\theta) = V\left[\frac{h^2}{2}\frac{dp}{dx}\left(\frac{y^2}{h^2} - \frac{y}{h}\right) - \frac{y}{h} + 1\right] \tag{1}$$

$$V_r(r,\theta) = \frac{Vh_{max}}{2\pi R_1}\frac{dh}{dx}\left(2 - 3\frac{h_m}{h}\right)\left(\frac{y^3}{h^3} - \frac{y^2}{h^2}\right) \tag{2}$$

where $V = \Omega R_1$ is the linear velocity of the inner cylinder, $h_{max} = R_2 - R_1 + e$ is the maximum gap, $h_m = (R2 - R1)/2$ is the mean gap, and h is the angle-dependent gap:

$$h = c(1 + \varepsilon\cos\theta) \tag{3}$$

where $c = R_2 - R_1$ is the clearance, $\epsilon = {}^{e}/_{c}$ is the eccentricity ratio, and y is measured radially from the inner cylinder as

$$y = c_p(1 + \varepsilon\cos\theta) \tag{4}$$

where $c_p = r - R_1$. The pressure gradient in Eq. (1) is given as

$$\frac{dp}{dx} = \frac{6(-\varepsilon \cos\theta + A)}{1 - \epsilon \cos\theta} \tag{5}$$

where $A = 3\epsilon^2/(2+\epsilon^2)$.

In this work, we choose R_1 = 55 and R_2 = 60 where these values are in units of polymer coil size [1]. Dimensionless units are used to maintain the validity of the assumption used to derive the velocity profile based on the lubrication theory for a "small" clearance space such that $c/R_1 \leq 0.1$.

3. Dimensionless Numbers

As mentioned before, the migration pattern of polymers in solution can be influenced by the degree of confinement experienced by the polymer as well as by the stress gradient over its dimension. Here, we define a dimensionless gradient number Gd to quantify the ratio of the polymer size to the distance d over which appreciable variations of stress or velocity gradient is expected to occur:

$$Gd = \sqrt{\frac{2\langle R^2\rangle_0}{3d^2}} \tag{6}$$

where $\langle R^2\rangle_0$ is the mean-square of end-to-end distance of the dumbbell in the absence of flow, $d = (c - e)$ is the minimum gap between the two cylinders, where a steep change in velocity gradient is expected in the eccentric cylinder. In addition, a dimensionless Weissenberg number Wi is defined to determine the ability of the flow to deform polymer molecules as

$$Wi = \frac{V\tau}{d} \tag{7}$$

where τ is the stress relaxation time of the polymer calculated as $\tau = \langle R^2\rangle_0/24D$ and D is the diffusion coefficient of the dumbbell calculated as $D = k_BT/(2\zeta)$, where ζ is the drag coefficient of the dumbbell bead and k_BT is the thermal energy. Moreover, in addition to Gd and Wi, a third relevant dimensionless group, i.e., Peclet number Pe, is defined as the ratio of the advective to diffusive transports of polymers under flow as

$$Pe = \frac{Vd}{D} \tag{8}$$

The three dimensionless numbers are related to each through below expression

$$Wi = \frac{V\tau}{d} = \frac{1}{24}\frac{\langle R^2\rangle_0}{d^2}\,Pe = \frac{1}{16}\,Gd^2\,Pe \tag{9}$$

The Hookean spring constant is defined as $H = 3k_BT/\langle R^2\rangle_0$ which can be related to Gd as $Gd^2 = \frac{2k_BT}{d^2H}$ and to Wi as $Wi = \frac{V\zeta}{4dH}$, where more details are available in [23]. For a completely analytical solution to be derived, all three dimensionless numbers need to remain small. Our previous work [23] showed that, for arbitrary Pe, although an analytical solution is not available, if Gd and Wi are small, a simplified polymer transport equation can be derived. In fact, as long as Gd remains small, concentration field equations can still be derived even if neither Pe nor Wi is small. This is explained in more detail in section 4.

4. Perturbation Theory

Our recent perturbation theory has been shown to successfully capture the stress-gradient-induced polymer migration in dilute solutions [23]. The theory includes coupled equations for polymer rheology, fluid dynamics and polymer mass transport. A flowchart summarising different levels of continuum theories and mesoscopic simulations for the stress-gradient-induced migration in dilute polymer solution is given in Figure 2 (reproduced from [9]). A Hookean dumbbell model in a very dilute solution is used and hydrodynamic interactions (HI) are neglected in this study. Note that HI can produce polymer migration as shown by earlier studies [26, 27], although without HI polymer migration can still occur [7]. The present theory focuses on the simplest case of dilute dumbbells without HI as a starting point for exploring the mechanisms of stress-gradient-induced polymer migration [23]. A more complete theory including HI can be developed in the future, and has been presented already for a simpler flow field with stress-gradient-induced polymer migration [9]. For small enough gradient number Gd, a continuum theory is valid for predicting polymer migration with different levels of perturbation. At small velocity, the Weissenberg number (Wi) expansion of the constitutive equation can be used. At high enough velocity, the Weissenberg number Wi expansion fails and to obtain the overall migration mass flux, the polymer conformation tensor S_{jk} needs to be obtained via solving a constitutive equation. Note that a wall-depletion term can be included within different levels of continuum theory to study the influence of wall-depletion-induced polymer migration. For a large gradient number Gd, the continuum theory fails, and mesoscopic simulation is required, which is the subject of our future study, where

we will develop a multiscale simulation formalism that couples molecular dynamics simulations [28-30] to a mesoscopic smoothed dissipative particle dynamics simulation [31-33] to capture the effects of hydrodynamics interactions and strong confinement on polymer configuration and migration.

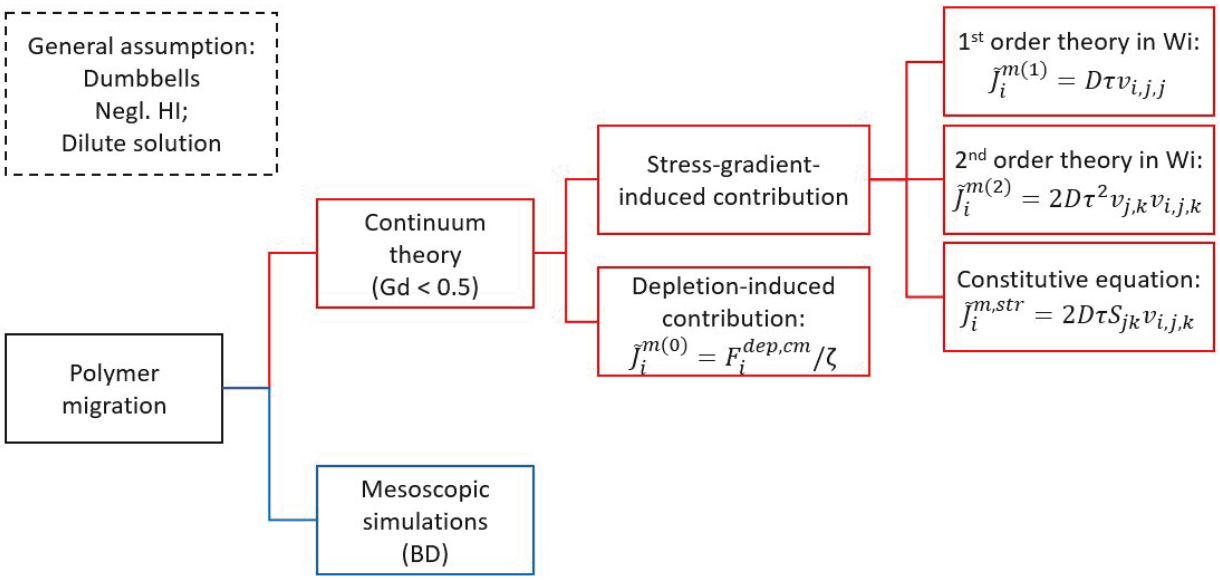

Figure 2 Flowchart summarising different levels of continuum theory and mesoscopic simulations for stress-gradient-induced migration in a dilute polymer solution (reproduced from [9])

Different levels of perturbation theories can be applied to predict polymer migration in dilute solutions. At the lowest order in gradient number Gd, the migration flux of a dilute Hookean dumbbell is given as

$$\tilde{J}_i^m = 2D\tau S_{jk} v_{i,j,k} + F_i^{dep,cm}/\zeta \tag{10}$$

where $F_i^{dep,cm}$ is the depletion force acting on the polymer's centre of mass, ζ is the bead drag coefficient, and $S_{ij} = \beta^2 \langle R_i R_j \rangle$ is the conformation tensor where R_i is the end-to-end distance of a dumbbell, the brackets "$\langle\ \rangle$" represent the ensemble average, and $\beta^2 = \frac{3}{2\langle R^2 \rangle_0}$ where the subscript "0" denotes that the average is in the absence of flow. The conformation tensor S_{ij} can be obtained by solving the upper-convected Maxwell equation given as

$$\dot{S}_{ij} = v_{i,k} S_{kj} + S_{ik} v_{j,k} - 1/\tau \left(S_{ij} - 1/2\, \delta_{ij} \right) \tag{11}$$

Where the over-dot represents the substantial time derivative, and the velocity v and its gradients in the above are expressed using Einstein notation. The first term in Eq. (10) represents migration due to variations in velocity gradients, while the second term denotes the depletion-induced migration from the walls. Note that earlier work showed that Eq. (10) gives the migration flux up to second order in Gd.

We now expand the upper-convected Maxwell Eq. (11) in the magnitude of the velocity gradient [1], which gives the following lowest order terms for the migration flow, including a zeroth-order migration flux in the depletion region:

$$\tilde{m}_i^{(0)} = F_i^{dep,cm} / \zeta \tag{12}$$

$$\tilde{m}_i^{(1)} = D\tau v_{i,j,j} \tag{13}$$

$$\tilde{m}_i^{(2)} = 2D\tau^2 v_{j,k} v_{i,j,k} \tag{14}$$

To seek solutions to the concentration field, these flux expressions can be used in the following steady-state convection-diffusion equation

$$-Dc_{,i,i} + v_i\, c_{,i} + (c\,\tilde{m}_i)_{,i} = 0 \tag{15}$$

As described in [23], we expand the concentration c in a Taylor's series in powers of the velocity magnitude V as $c = c^{(0)} + c^{(1)} + c^{(2)} + \cdots$ with each term proportional to V raised to the power in the parenthetical exponent. This can be considered an expansion in the Peclet number Pe. Similar expansion can be achieved in the Wi, considering each term to be proportional to the magnitude of the relaxation time raised to the power in the parenthetical exponent [23].

4.1 In the absence of wall depletion:

When wall-depletion is not included, only the stress-gradient-induced migration occurs. Therefore, in the absence of any repulsion from the vicinity of the walls, there is no zeroth-order migration flux and $c^{(0)} = \bar{c}$ is a constant. For eccentric cylinders in the absence of HI and wall depletion and in dilute regimes, and when both Wi and Pe are small, the steady-state governing equation gives the first order theory in Pe as

$$-Dc_{,i,i}^{(1)} + v_i\, c_{,i}^{(0)} + \left(c^{(0)}\, \tilde{m}_i^{(1)}\right)_{,i} = 0 \tag{16}$$

where the gradient of the constant $c^{(0)}$ is zero, making the second term in Eq. (16) equal to zero. This also reduces the third term in Eq. (16) to $c^{(0)}\, \tilde{m}_{i,i}^{(1)} = c^{(0)} D\tau v_{i,j,j,i}$. Using the continuity equation $v_{i,i} = 0$, we can get $v_{i,j,j,i} = 0$, which then implies that the third term in Eq. (16) is also zero. $c^{(1)}$ is thus zero and there is no first-order contribution to the concentration field, so that the lowest-order concentration variation is proportional to Wi^2, as discussed in [1].

The second order theory in Pe is expressed as

$$-Dc_{,i,i}^{(2)} + v_i\, c_{,i}^{(1)} + \left(c^{(0)}\, \tilde{m}_i^{(2)}\right)_{,i} + \left(c^{(1)}\, \tilde{m}_i^{(1)}\right)_{,i} = 0 \tag{17}$$

In the absence of wall-induced migration, we showed that $c^{(1)} = 0$, hence the second term in Eq. (17) is zero. The third term in Eq. (17) is the source term for 2nd order stress-gradient-induced migration. The fourth term in Eq. (17) is zero as both $c^{(1)}$ and $\tilde{m}_{i,i}^{(1)}$ are zero. Therefore, Eq. (17) can be simplified as below

$$-Dc_{,i,i}^{(2)} + 2D\tau^2 \bar{c} v_{j,k,i} v_{i,j,k} = 0 \tag{18}$$

To study situations where $Pe > 1$ with $Wi << 1$, we cannot carry out an expansion in Pe but we can use the perturbation in Wi [23]. Therefore, following the same procedure used for the expansion in Pe, we get at lowest order (second order) in Wi

$$-Dc_{,i,i}^{(2)} + v_i\, c_{,i}^{(2)} + 2D\tau^2 \bar{c} v_{j,k,i} v_{i,j,k} = 0 \tag{19}$$

Note that Eq. (19) is identical to the second-order equation from the Peclet number expansion, Eq. (18), except that Eq. (19) contains the convection term $v_i\, c_{,i}^{(2)}$ which is missing from Eq. (18), because this term is third order in Pe, even though it is only second order in Wi. As long as $Wi << 1$, Eq. 19 is valid for arbitrary *Pe*. In cylindrical coordinates Eq. (19) becomes

$$-D\left(\frac{\partial^2 c^{(2)}}{\partial r^2} + \frac{1}{r}\frac{\partial c^{(2)}}{\partial r} + \frac{1}{r^2}\frac{\partial^2 c^{(2)}}{\partial \theta^2}\right) + v_r\, \frac{\partial c^{(2)}}{\partial r} + v_\theta \frac{1}{r}\frac{\partial c^{(2)}}{\partial \theta} + 2D\tau^2 \bar{c} v_{j,k,i} v_{i,j,k} = 0 \tag{20}$$

The migration terms in Eq. (18) and Eq. (19) as well as the first order and high order derivatives of the velocity components in cylindrical coordinates [34] are given in the Appendix I.

At high enough velocity, the Weissenberg number expansion of the constitutive equation fails, and the constitutive Eq. (11) must be solved numerically for the conformation tensor S_{ij}, which is then used in Eq. (10) for the overall migration flux $\tilde{j}_i^m$ which when substituted into Eq. (15) gives the following equation for the polymer concentration for any Wi:

$$-Dc_{,i,i} + v_i\, c_{,i} + 2D\tau\left(cS_{jk}v_{i,j,k}\right)_{,i} = 0 \tag{21}$$

In cylindrical coordinates, Eq. (21) becomes

$$-D\left(\frac{\partial^2 c}{\partial r^2} + \frac{1}{r}\frac{\partial c}{\partial r} + \frac{1}{r^2}\frac{\partial^2 c}{\partial \theta^2}\right) + v_r\,\frac{\partial c}{\partial r} + v_\theta \frac{1}{r}\frac{\partial c}{\partial \theta} + \frac{\partial c}{\partial r}\left[2D\tau S_{jk}v_{r,j,k}\right] + \frac{1}{r}\frac{\partial c}{\partial \theta}\left[2D\tau S_{jk}v_{\theta,j,k}\right] + c[2D\tau S_{jk,i}v_{i,j,k}] = 0 \tag{22}$$

while Eq. (11) reduces to the system of equations given below

$$\begin{cases} S_{rr}\left(2v_{r,r} - \frac{1}{\tau}\right) + S_{r\theta}\left(2v_{r,\theta} + \frac{2v_\theta}{r}\right) = v_r\,\frac{\partial S_{rr}}{\partial r} + \frac{v_\theta}{r}\frac{\partial S_{rr}}{\partial \theta} - \frac{1}{2\tau} \\ S_{rr}\left(v_{\theta,r} - \frac{v_\theta}{r}\right) + S_{r\theta}\left(v_{r,r} + v_{\theta,\theta} - \frac{1}{\tau}\right) + S_{\theta\theta}\left(v_{r,\theta} + \frac{v_\theta}{r}\right) = v_r\,\frac{\partial S_{r\theta}}{\partial r} + \frac{v_\theta}{r}\frac{\partial S_{r\theta}}{\partial \theta} \\ S_{r\theta}\left(2v_{\theta,r} - \frac{2v_\theta}{r}\right) + S_{\theta\theta}\left(2v_{\theta,\theta} - \frac{1}{\tau}\right) = v_r\,\frac{\partial S_{\theta\theta}}{\partial r} + \frac{v_\theta}{r}\frac{\partial S_{\theta\theta}}{\partial \theta} - \frac{1}{2\tau} \end{cases} \tag{23}$$

We implement periodic boundary conditions in the θ-direction at $\theta = 0$ and $\theta = 2\pi$ to ensure the concentration at these two values of θ are equal to each other. We use a no-flux condition in the r-direction at the location of two solid boundaries, i.e., $r = R_1$ and $r = R_2$. For the no-flux boundary condition, we obtain the radial flux terms from Eq. (21) and set their sum to zero at both cylinder boundaries, i.e., inner cylinder boundary and outer cylinder boundary, as given below

$$\frac{\partial c}{\partial r} - c\left(\frac{1}{D}v_r + 2\tau S_{jk}v_{r,j,k}\right) = 0 \tag{24}$$

4.2 In the presence of wall depletion

In the presence of wall depletion, in contrast to section 4.1 which considered only the stress-gradient-induced migration, the depletion force results in a non-uniform concentration field at zeroth order, $c^{(0)}$. A decaying-exponential potential [35] is used to approximate the depletion, expressed as $U^{dep}(r) = \lambda \exp\left[-\left(\frac{h}{2} - \left|r - \frac{R_1+R_2}{2}\right|\right)/R_d\right]$ where r is the radial coordinate centered at the axis of rotation, R_d is a fitted length scale proportional to the radius of gyration of the

polymer dumbbell and the interaction strength λ is adjusted to match the depletion observed in BD simulations of the same system [1]. The depletion force is directed normal to the walls and given as $F_i^{dep,cm} = -\frac{dU^{dep}}{dr}$, producing the flux in Eq. (12). The coupling of the depletion layer to the velocity produces what we elsewhere referred to as "depletion-convection-induced" migration [36]. When polymer depletion results in a non-uniform $c^{(0)}$, the fluxes do not in general vanish and one obtains a first order concentration variation. We can go to higher orders by incorporating more terms into the Taylor's series expansion of the overall concentration field.

This depleted concentration field can be obtained by retaining only the zeroth-order terms in Wi in Eq. (15)

$$-Dc_{,i,i}^{(0)} + \left(c^{(0)}\,\tilde{m}_i^{(0)}\right)_{,i} = 0 \tag{25}$$

where $\tilde{m}_i^{(0)}$ is found from Eq. (12). Note that since the wall depletion force is axisymmetric, $\tilde{m}_\theta^{(0)}$ is zero and therefore $c^{(0)}$ is independent of θ, although it depends on r. In cylindrical coordinates, Eq. (25) becomes

$$-D\frac{\partial^2 c^{(0)}}{\partial r^2} + c^{(0)}\frac{\partial \tilde{j}_r^{m(0)}}{\partial r} + \tilde{m}_r^{(0)}\frac{\partial c^{(0)}}{\partial r} = 0 \tag{26}$$

Since in the presence of the zeroth-order wall potential, the zeroth-order concentration is not uniform, the first order concentration $c^{(1)}$ therefore is computed including both the 0th order contribution and the 1st order migration flux, in contrast to that in section 4.1. To obtain the first order contribution to the polymer concentration field (i.e., the contribution proportional to Wi), we consider all first order terms in Eq. (15) yielding

$$-Dc_{,i,i}{}^{(1)} + v_i\, c_{,i}{}^{(0)} + \left(c^{(0)}\,\tilde{m}_i^{(1)}\right)_{,i} + \left(c^{(1)}\,\tilde{m}_i^{(0)}\right)_{,i} = 0 \tag{27}$$

where $\tilde{m}_i^{(1)}$ is given in Eq. (13). Note that the second term in this equation is the convective contribution, which is proportional to the Peclet number Pe. In cylindrical coordinates, Eq. (27) becomes

$$-D\left(\frac{\partial^2 c^{(1)}}{\partial r^2}+\frac{1}{r}\frac{\partial c^{(1)}}{\partial r}+\frac{1}{r^2}\frac{\partial^2 c^{(1)}}{\partial \theta^2}\right)+v_r\frac{\partial c^{(0)}}{\partial r}+v_\theta\frac{1}{r}\frac{\partial c^{(0)}}{\partial \theta}+\left[\frac{\partial}{\partial r}\left(c^{(0)}\tilde{m}_r^{(1)}\right)+\frac{1}{r}\frac{\partial}{\partial \theta}\left(c^{(0)}\tilde{m}_\theta^{(1)}\right)\right]+\left[\frac{\partial}{\partial r}\left(c^{(1)}\tilde{m}_r^{(0)}\right)+\frac{1}{r}\frac{\partial}{\partial \theta}\left(c^{(1)}\tilde{m}_\theta^{(0)}\right)\right]=0 \tag{28}$$

After solving $c^{(0)}$ and $c^{(1)}$, the second order contribution $c^{(2)}$ can also be calculated by solving the corresponding convection-diffusion equation

$$-Dc_{,i,i}^{(2)}+v_i\,c_{,i}^{(1)}+\left(c^{(0)}\tilde{m}_i^{(2)}\right)_{,i}+\left(c^{(1)}\tilde{m}_i^{(1)}\right)_{,i}+\left(c^{(2)}\tilde{m}_i^{(0)}\right)_{,i}=0 \tag{29}$$

In cylindrical coordinates, Eq. (29) becomes

$$-D\left(\frac{\partial^2 c^{(2)}}{\partial r^2}+\frac{1}{r}\frac{\partial c^{(2)}}{\partial r}+\frac{1}{r^2}\frac{\partial^2 c^{(2)}}{\partial \theta^2}\right)+v_r\frac{\partial c^{(1)}}{\partial r}+v_\theta\frac{1}{r}\frac{\partial c^{(1)}}{\partial \theta}+\left[\frac{\partial}{\partial r}\left(c^{(0)}\tilde{m}_r^{(2)}\right)+\frac{1}{r}\frac{\partial}{\partial \theta}\left(c^{(0)}\tilde{m}_\theta^{(2)}\right)\right]+\left[\frac{\partial}{\partial r}\left(c^{(1)}\tilde{m}_r^{(1)}\right)+\frac{1}{r}\frac{\partial}{\partial \theta}\left(c^{(1)}\tilde{m}_\theta^{(1)}\right)\right]+\left[\frac{\partial}{\partial r}\left(c^{(2)}\tilde{m}_r^{(0)}\right)+\frac{1}{r}\frac{\partial}{\partial \theta}\left(c^{(2)}\tilde{m}_\theta^{(0)}\right)\right]=0 \tag{30}$$

For concentric cylinders (Taylor-Couette flow) [1], the terms involving $c^{(1)}$ disappear because the first order concentration $c^{(1)}$ vanishes, even when axisymmetric wall depletion exists. In eccentric cylinders with wall depletion, $c^{(1)}$ does not vanish because $c^{(0)}$ is non-uniform as flow component normal to the wall now exists. Eq. (30) for $c^{(2)}$ can be solved using the zeroth-order concentration $c^{(0)}$ obtained from solving Eq. (26), the first order concentration $c^{(1)}$ obtained from solving Eq. (28) and the migration flux terms $\tilde{m}_i^{(0)}$, $\tilde{m}_i^{(1)}$ and $\tilde{m}_i^{(2)}$ from Eqs (12), (13) and (14), respectively.

At high enough velocity, the Weissenberg number expansion of the constitutive equation fails and the constitutive theory needs to be used. Therefore, Eq. (15) needs to be solved by using the overall migration flux including wall-depletion-induced contribution as

$$-Dc_{,i,i}+v_i\,c_{,i}+\left[c\left(2D\tau S_{jk}v_{i,j,k}+F_i^{dep,cm}/\zeta\right)\right]_{,i}=0 \tag{31}$$

in cylindrical coordinates Eq. (31) becomes

$$-D\left(\frac{\partial^2 c}{\partial r^2}+\frac{1}{r}\frac{\partial c}{\partial r}+\frac{1}{r^2}\frac{\partial^2 c}{\partial \theta^2}\right)+v_r\frac{\partial c}{\partial r}+v_\theta\frac{1}{r}\frac{\partial c}{\partial \theta}+\frac{\partial c}{\partial r}\left[2D\tau S_{jk}v_{r,j,k}+\frac{{}_r^{dep,cm}}{\zeta}\right]+\frac{1}{r}\frac{\partial c}{\partial \theta}\left[2D\tau S_{jk}v_{\theta,j,k}+\frac{{}_\theta^{dep,cm}}{\zeta}\right]+c\left[2D\tau S_{jk,i}v_{i,j,k}+\frac{1}{\zeta}\frac{\partial\,{}_r^{dep,cm}}{\partial r}+\frac{1}{\zeta}\frac{1}{r}\frac{\partial\,{}_\theta^{dep,cm}}{\partial \theta}\right]=0 \tag{32}$$

Periodic boundary conditions in the θ-direction at $\theta = 0$ and $\theta = 2\pi$ are implemented to ensure the concentration at these two values of θ equal to each other. No-flux in the r-direction at the location of two solid boundaries, i.e., $r = R_1$ and $r = R_2$ are again used. For the no-flux boundary condition, we set the total flux in the r-direction to zero and add the wall-depletion term so that Eq. (24) becomes

$$\frac{\partial c}{\partial r} - c\left(\frac{1}{D}v_r + 2\tau S_{jk}v_{r,j,k} + \frac{1}{D}\frac{\overset{dep,cm}{r}}{\zeta}\right) = 0 \tag{33}$$

here, and k are dummy variables, representing r or θ.

At high enough velocity, the Weissenberg number expansion of the constitutive equation fails. In such cases, Eqs. (13,14) are no longer useful, and constitutive Eq. (11) must be solved for the conformation tensor S_{ij}, which is then used in Eq. (10) to obtain the overall migration flux at all Wi. Beyond this, if the size of the polymer is comparable to the geometrical length scale, i.e. when Gd becomes large, the use of continuum theory based on low-order expansions in Gd fails altogether, and mesoscopic simulation methods that track individual polymer molecules are needed.

5. Results and Discussion

A finite difference method is applied to discretize the continuum theory equations given in Section 4. A mesh size of 200 × 200 is used to represent steps in the radial and azimuthal directions, respectively. The central difference scheme is implemented for discretization in the azimuthal direction as well as in the radial direction, while boundary cells in the radial direction uses a forward difference for the inner boundary at r=R_1 and a backward difference for the outer boundary at r=R_2. The initial field of the polymer concentration is set to be unity. A matrix algebra technique is used to solve the linearized equations, where cells in the radial direction range from i = 1 to 200 and cells in the azimuthal direction range from j = 1 to 200. The first solution starts from cell (2, 2) using central difference method, i.e. interpolating values from its adjacent cells (1, 2), (3, 2), (2, 1), (2, 3); and then iterate through all cells in the computational domain. For the constitutive equation, the initial field of conformation tensor is set to unity and similar matrix algebra technique

is used to compute conformation tensor in the computational domain and converged solution is then used to solve the polymer concentration. The spatial domain is discretised as described and time interval is not included in this work. A converged solution is achieved after 10000 iterations for each simulation. For $Wi > 1$, an under-relaxation parameter η is implemented for calculating the conformation tensor S_{ij} through Eq. (23) to avoid steep changes in S_{ij} values between subsequent iterations. This allows stable calculations when Wi and subsequently Pe become large (which leads to large convection and strong flow deformation of polymer molecules). To maintain computational efficiency, a minimum value of η=0.1 is applied, since a smaller η leads to stronger under-relaxation and therefore, longer calculations. Converged simulation results are analysed to show the capability of the continuum theories. More details of the numerical methods used are available in Appendix II.

5.1. Stress-gradient-induced migration

We first neglect the wall effect, and evaluate the concentration field at different levels of perturbation theory defined in section 4.1. We follow the flowchart for stress-gradient-induced continuum migration theories for incompressible fluids presented in Figure 2 to investigate the validity of different levels of perturbation theories for polymer migration in eccentric cylinders.

Comparison between concentric and eccentric cylinders (with eccentricity $e = 1$, which corresponds to $\epsilon = {}^{e}/_{c}$ = 0.2, or 20% of the gap) is firstly presented using constitutive theory. Constitutive theory is used as the default method throughout this work unless otherwise specified. To show the reliability of the current theory we first reproduce concentric cylinder results (by setting eccentricity $e = 0$) and then demonstrate the impact of eccentricity on polymer migration. Here we note that polymer concentration C is normalized by Wi^2 as $C = (C - 1)/Wi^2$ to better present the variation of concentration profile in section 5.1, when only stress-gradient-induced migration is included and C is very close to unity for small Wi. This normalization is not performed in section 5.2, when stress-gradient-induced and wall-depletion-induced migration are both included.

Figure 3 shows the predicted steady-state distribution of polymer concentration C in the radial direction at four different azimuthal angles resulting from polymer migration. Polymer has migrated towards the inner cylinder for both concentric and eccentric cylinders. As expected, for concentric cylinders in Figure 3(a), the polymer concentration profiles at the four azimuthal angles are identical. For eccentric cylinders in Figure 3(b), the concentration profile is steeper near the outer cylinder at $\theta = 0$, i.e. in the wider clearance region (see Figure 1), while at other azimuths, at $\theta = \pi/2, \pi, 3\pi/2$, the higher concentration gradient $C/\ y$ is in the inner half of the clearance, indicating steeper polymer build up near inner cylinder. Note that in Figure 3(b) the position y within the gap is not normalized by the local gap $h(\theta)$ so that the angle-dependence of clearance due to eccentricity is shown at various azimuthal angles θ. A normalized radial position $y/h(\theta)$ will be used thereafter. For example, for eccentricity $e = 1$, $h(\theta)$ = 6 at $\theta = 0$ and $h(\theta)$= 4 at $\theta = \pi$.

Figure 4 shows the distribution of polymer concentration C in the circumferential direction at three different normalized radial distances $y/h(\theta)$, i.e., near the inner cylinder, in the middle of the gap, and near the outer cylinder. Higher concentrations are observed towards the inner cylinder, as in Figure 3, but with the influence of eccentricity at different θ values clearly shown in Figure 4(b).

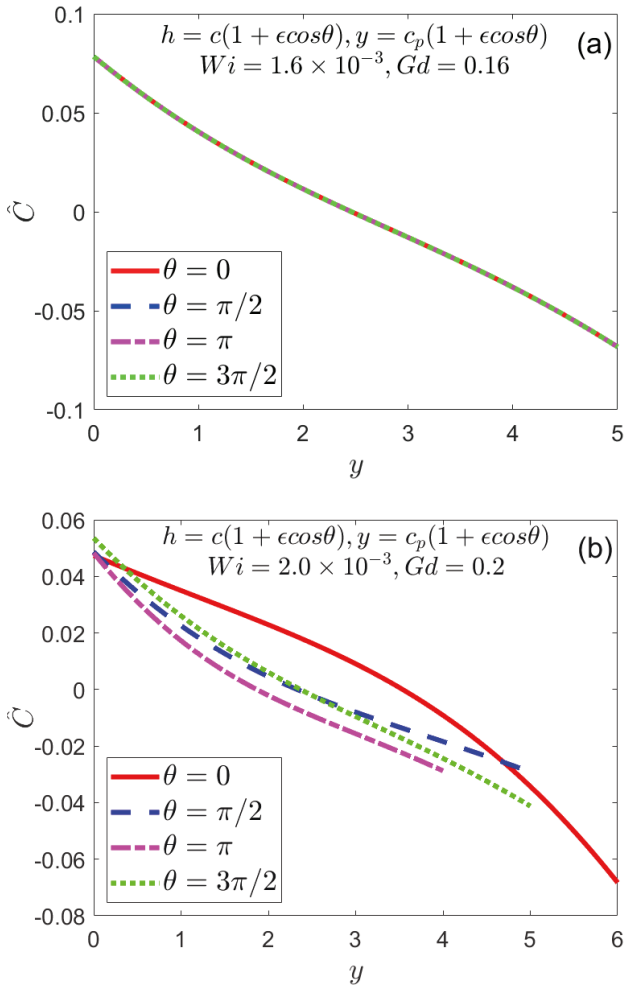

Figure 3. Radial profile of scaled polymer concentration $\widehat{\boldsymbol{C}}$ for eccentricity (a) = and (b) =

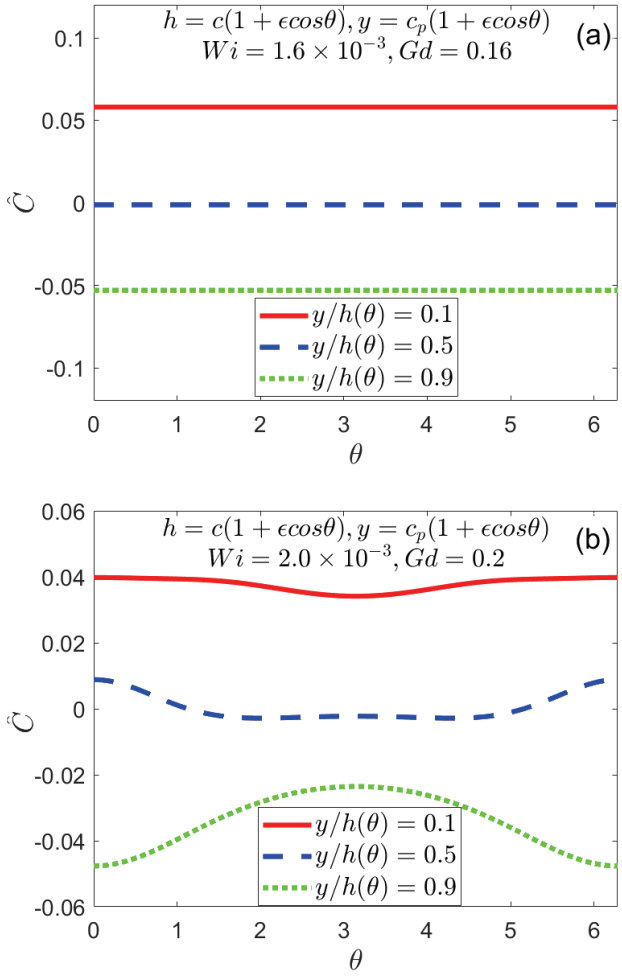

Figure 4. Profile of scaled polymer concentration $\widehat{\boldsymbol{C}}$ in the circumferential direction for eccentricity (a) = and (b) =

Next, maintaining a constant eccentricity of $e = 1$, the rotational velocity of the inner cylinder is increased from 0.001 to 0.2, resulting in an increase of Peclet number Pe from 0.08 to 15.1, while keeping the Weissenberg number $Wi < 1$. The gradient number Gd remains constant at 0.2. This is conducted to study the effect of convection in terms of Pe. Note here we used second order theory in Wi (Eq. 19) and the second order theory in Pe (Eq. 18) to perform the numerical calculations, providing for the effect of convection to be isolated. Figure 5(a & b) shows the distribution of C in the radial and circumferential directions, respectively. Figure 5(a) shows that in the radial direction C profile calculated through (Eq. 19) closely match that calculated from the (Eq. 18) as Pe increases to 15.1. In the circumferential direction at $y/h(\theta) = 0.0$, Figure 5(b) shows that C profile remains largely unchanged when $Pe < 1$ and matches that calculated from

(Eq. 18) . However, when $Pe > 1$, C profile calculated from Eq. 19 shows deviations in the wide gap area i.e., $\theta = 0$ from C profile calculated from Eq. 18. Note that the increase in Pe produced by an increase of the inner cylinder rotation speed also leads to an increased Weissenberg number $Wi = \frac{1}{16} Gd^2 Pe$, though in Figure 5 we keep $We < 1$ to isolate the effect of Pe. When $Pe > 1$, the influence of convection kicks in and alters the polymer concentration profile, changing local C value. The low order continuum theory remains valid for large Pe, reaffirming the previous finding that the simplified polymer transport equation is valid for arbitrary Pe when Gd and Wi are both small [1].

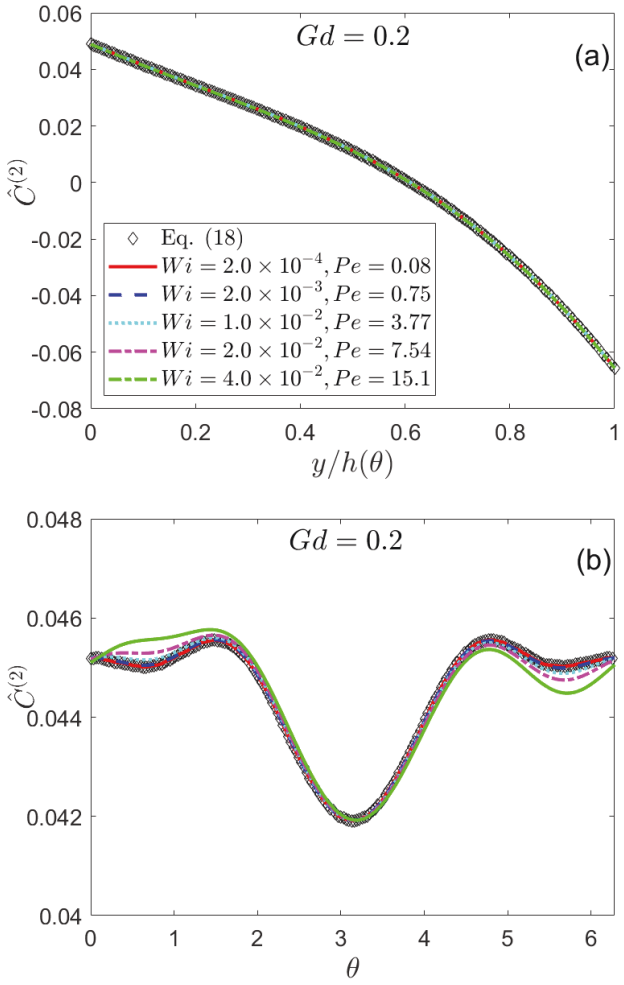

Figure 5 Profile of C from 2nd order theory in Wi (lines) and 2nd order theory in Pe (symbols) in the (a) radial direction at = and (b) in the circumferential direction at $\boldsymbol{y/h}$( ) = . (sharing the same legend in (a)) for different $\boldsymbol{Wi}$ with eccentricity =

Figure **6** compares the radial distribution of C at $\theta = 0$ and the velocity field for eccentric cylinders with eccentricity = calculated using the constitutive theory and the second order theory in Wi given in flowchart in Figure 2 and Equations (21) & (19), respectively. At Wi = 2.0×10^{-4}, polymer concentration obtained from the second order theory matches well with that from the constitutive theory as shown in Figure 6(b). Results from the two levels of the theory match well for each Wi respectively, showing higher polymer concentration towards the inner cylinder. When Wi approaches unity, both theories predict reduced C values from $y/h(\theta) = 0.2$ to 0.8 compared to those from small Wi conditions, showing the influence of convection on concentration profile. (The lower overall concentration at $\theta = 0$ for increased Wi is compensated by a higher overall concentration at other values of θ.) When Wi further increases above unity, the calculation using the constitutive theory becomes numerically unstable, yielding an oscillatory distribution C in the circumferential direction. This oscillation initiates from $\theta = 0$ near the inner cylinder and propagates downstream circumferentially with increasing numbers of iterations in the calculation, eventually diverging. An under-relaxation parameter η, therefore, is implemented to stabilize the calculation, which allows attainment of converged solutions up to a maximum value of $Wi = 1.6$ for the constitutive theory calculation when under-relaxation parameter is allowed to go as low as η=0.1. At higher Wi the numerical instability amplifies, requiring an excessively low under-relaxation parameter, which is computationally inefficient. This calculation instability observed at higher Wi is possibly due to amplified numerical artefacts.

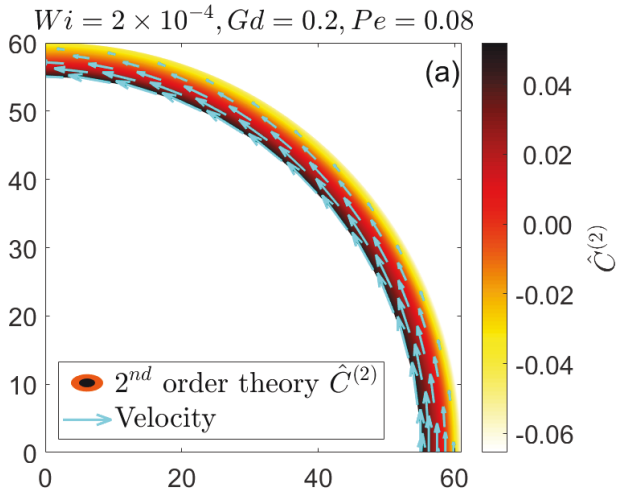

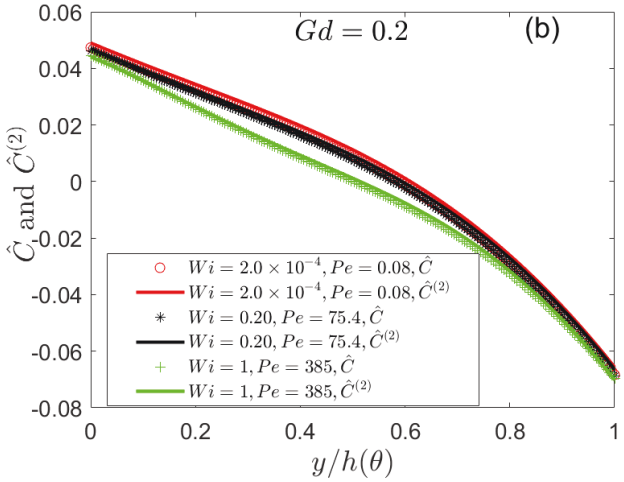

Figure 6. Concentration contour map in the gap between eccentric cylinders with eccentricity = of (a) second order theory concentration $\widehat{\boldsymbol{C}}^{(2)}$ when $\boldsymbol{Wi} = \boldsymbol{2} \times$ ⁻ and (b) radial concentration profile at = predicted by both theories when $\boldsymbol{Wi} = \boldsymbol{2} \times$ ⁻ , $\boldsymbol{Wi} =$ **.2** and $\boldsymbol{Wi} =$ respectively.

Next, Figure 7 explores the effect of eccentricities of $e = 1 - 4$ for Wi = 2.0×10^{-3} – 7.9×10^{-3}. Given that we define Gd using the thinnest gap, Gd changes from 0.2 to 0.81 as eccentricity increases. Figure 7(a) shows that at the widest gap i.e., $\theta = 0$, an increase in eccentricity beyond $e = 2$ leads to a non-monotonic concentration gradient, with positive $C/\ y$ from $y/h(\theta) = 0$ to 0. , and negative thereafter. At lower eccentricities, the maximum concentration C remains near the inner cylinder. This local maximum in C as a function of y can be further seen near $\theta = 0$ in Figure 8 at high $e = 3$ or 4. The non-monotonic concentration profile for large eccentricity is dictated by the variations of the migration term defined in Eq. (10), which is due to changes in the second order derivatives of the velocity components and in the conformation tensor. At low Wi, the migration is controlled by the second order derivatives of the velocity components, in the term $\nu_{j,k,i}\nu_{i,j,k}$ in Eq. (18). In the simplest case of concentric cylinders, polymers under tension on curved streamlines experience a net inward force and therefore an inward migration towards the centre of curvature. When eccentricity becomes large, there are multiple second order velocity derivatives that contribute to the net flux, and the net result is a non-monotonic profile. By way of analogy, we note that at high enough gap and high eccentricity, a recirculating flow occurs in eccentric cylinder flow, and under less severe conditions the velocity becomes non-monotonic in the gap, as it does at $e = 3$ or 4 in the problem considered here. So, it is not surprising that higher order velocity derivatives would also become non-monotonic with increasing eccentricity.

Figure 7(b) shows the distribution of polymer concentration C in the circumferential direction, at $y/h(\theta) = 0.2$, i.e., near the inner cylinder. At low eccentricities $e = 1$ 2, a "bell-shaped" C distribution is observed, with a maximum C near $\theta = 0$ and a minimum C near $\theta = \pi$; i.e. at the narrowest gap. At high eccentricities $e = 3$ 4, in addition to the minimum near $\theta = \pi$, two more

minima near $\theta = \pi/4$ and $\theta = \pi/4$ are observed. Moreover, the increased eccentricity leads to a decrease in C with increasing Wi near $\theta = 0$, although the value of C itself (without normalization by Wi^2) near $\theta = 0$ increases with increasing eccentricity. Note that Gd quantifies the ratio of polymer size to the minimum gap. An increased eccentricity therefore results in a larger Gd value, and the size of the polymer becomes more comparable to the narrow clearance. Figure 8 demonstrates an increasingly inhomogeneous concentration profile in the θ direction when eccentricity increases.

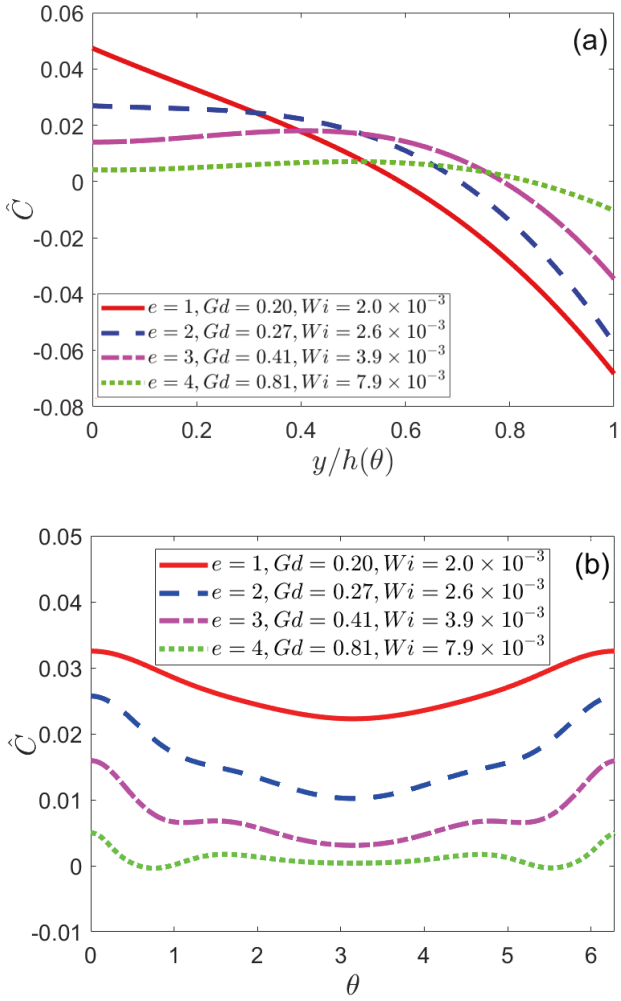

Figure 7 Profile $\widehat{\boldsymbol{C}}$ in the (a) radial direction at = and (b) circumferential direction at $\boldsymbol{y/h}(\ ) = \ .\mathbf{2}$ for eccentricities = ~

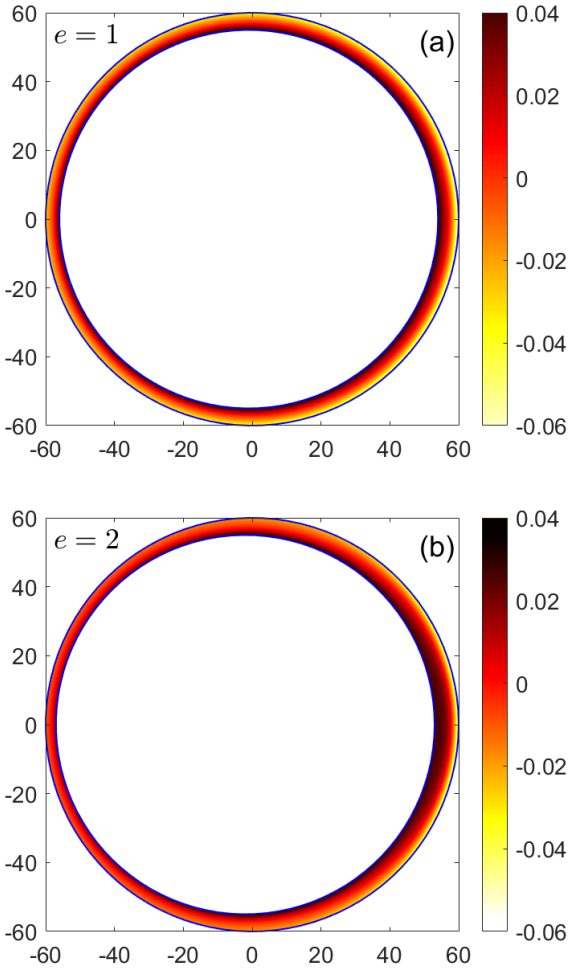
$e = 1$
(a)
60
40
20
0
-20
-40
-60
-60 -40 -20 0 20 40 60
0.04
0.02
0
-0.02
-0.04
-0.06
$e = 2$
(b)
60
40
20
0
-20
-40
-60
-60 -40 -20 0 20 40 60
0.04
0.02
0
-0.02
-0.04
-0.06

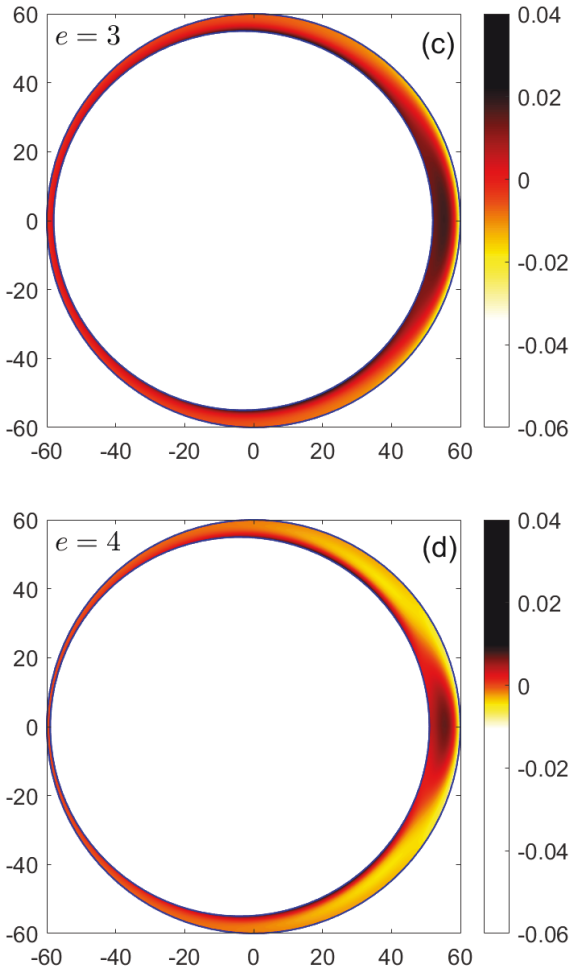

Figure 8 Contour plot of scaled polymer concentration $\widehat{\boldsymbol{C}}$ in the gap for eccentricities $= \sim$

Our results show that the low order theory remains valid when Wi number is small (shown in Figure **6**), but when Wi approaches 1, the constitutive theory should be used to take into account the effect of flow on the polymer conformation tensor, which is used to compute the migration flux. The low order theory predicts a monotonic increase in polymer concentration near the inner cylinder with increasing Wi, while the constitutive theory captures viscoelastic effects more fully by calculating the conformation tensor S_{ij} outside of the weak flow limit. However, the solution based on the constitutive equation becomes numerically unstable at large Wi values, eventually leading to unreliability of the continuum theory when $Wi > 1.6$ at least if the under-relaxation parameter is set no lower than η=0.1. Additionally, convection outside of the second order limit in Pe is found to influence the polymer concentration profile when $Pe > 1$. However, the 2nd order perturbation theory in Wi remains valid even for large Pe as long as Wi remains small. Gd

increases as eccentricity increases and the continuum theory for the eccentric cylinder system fails when Gd value approaches unity, i.e., when polymer size becomes comparable to the distance over which appreciable changes in stress or velocity gradient occur (i.e., there is strong confinement). For Gd approaching unity, mesoscopic simulations will be required to capture polymer migration, which is the subject of our future work, where we plan to couple molecular dynamics [37] simulations [38] with smoothed dissipative particle dynamics [33, 39] to design polymer-based lubricants with a variety of polymer chain structures and linear-dendrimer polymer blends [30].

5.2 Stress-gradient and depletion-induced migration

Previous studies showed that polymer migration due to wall steric depletion can be significant in confined channels [9]. (Note that the wall migration effects considered here are entirely due to steric depletion, and not to wall hydrodynamic interactions, which can also cause significant migration effects under flow [40, 41]). To understand the influence of wall steric depletion-induced polymer migration in eccentric cylinders, we now introduce wall-depletion terms into the governing equations by solving Eq. (32) using conformation [14] tensor S_{ij} obtained via the constitutive theory.

As shown in Eq. (10), the polymer migration flux is composed of two terms, i.e., the stress-gradient-induced contribution $\tilde{}^{m,str} = 2D\tau S_{jk}v_{i,j,k}$ and the wall-depletion-induced contribution $\tilde{}^{m,dep}_{r} = F_r^{dep,cm}/\zeta$. Figure 9 shows the distribution of migration fluxes from both terms in the radial direction, for eccentricity $e = 1$ at $\theta = 0$ and Wi = 0.47. Note that $\tilde{}^{m,dep}_{r}$ and ($\tilde{}^{m,dep}_{r}$ + $\tilde{}^{m,str}$) share the same y axis on the left, and $\tilde{}^{m,str}$ has its own y axis on the right. $\tilde{}^{m,str}$ decreases from $y/h(\theta) = 0$ to 1 and is negative, indicating the stress-gradient-induced migration is directed towards the inner cylinder. As expected, $\tilde{}^{m,dep}_{r}$ is largest in magnitude near each wall, and is nearly zero between $y/h(\theta) = 0.1$ to 0.9. $\tilde{}^{m,dep}_{r}$ near the inner cylinder is positive while near the outer cylinder it is negative, producing migration towards the centre of the gap. The magnitude of $\tilde{}^{m,dep}_{r}$ in the near-wall regions is almost 10^4 times higher than that of $\tilde{}^{m,str}$, indicating that $\tilde{}^{m,dep}_{r}$ dominates near the wall, as confirmed by the overlap of $\tilde{}^{m,dep}_{r}$ and ($\tilde{}^{m,dep}_{r}$ + $\tilde{}^{m,str}$).

Figure 10 shows the concentration distribution in the radial direction with and without wall-depletion, confirming by the near-zero concentration near the walls that $\tilde{J}_r^{m,dep}$ dominates there, as suggested also by Figure 9. Away from the walls, only a small concentration gradient $(C_{\tilde{J}_r^{m,dep}+\tilde{J}^{m,str}})/\ y$ is predicted, resulting from the effect of $\tilde{J}^{m,str}$ driving polymer migration towards the inner cylinder. In the absence of $\tilde{J}_r^{m,dep}$, only $\tilde{J}^{m,str}$ drives the polymer migration leading to an increased polymer concentration ($C_{\tilde{J}^{m,str}}$) towards the inner cylinder. Note that the largest value of $C_{\tilde{J}_r^{m,dep}+\tilde{J}^{m,str}}$ is significantly higher than that of $C_{\tilde{J}^{m,str}}$, due to significant contribution of $\tilde{J}_r^{m,dep}$, which drives polymer away from the walls.

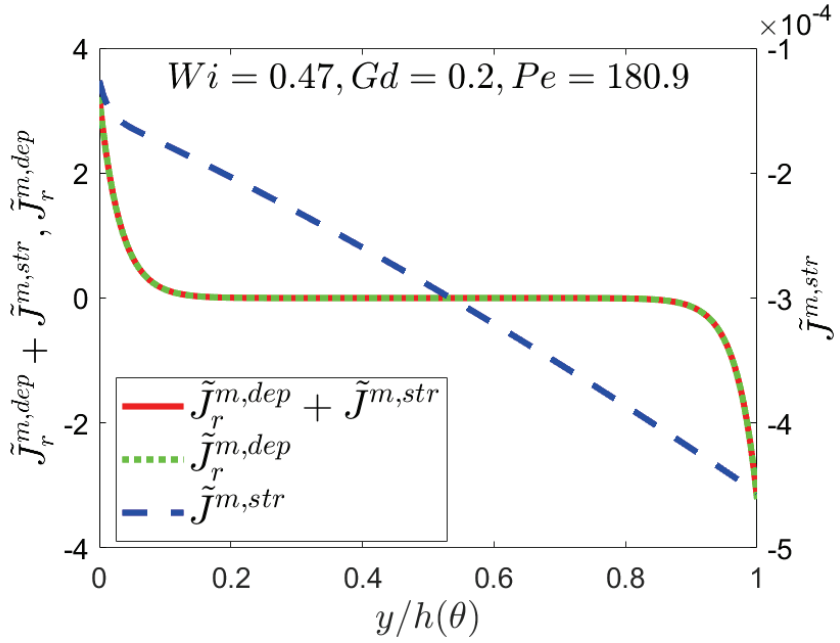

Figure 9 Gap dependence of migration flux of a dilute Hookean dumbbell due to wall-depletion-induced flux $\tilde{\boldsymbol{J}}_{\boldsymbol{r}}^{\boldsymbol{m,d\ p}}$ and stress-gradient-induced flux $\tilde{\boldsymbol{J}}^{\boldsymbol{m,str}}$ for eccentricity = at = . The sum of the two (red solid line) overlaps with $\tilde{\boldsymbol{J}}_{\boldsymbol{r}}^{\boldsymbol{m,d\ p}}$ (dashed green line) since the stress gradient terms is so small (note the re-scaling by 10^{-4} on the right axis).

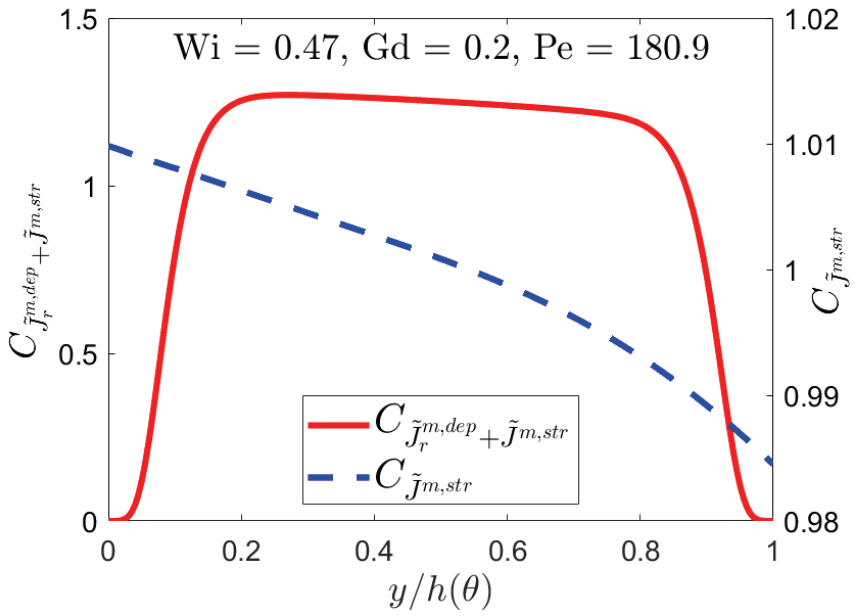

Figure 10 Radial distribution of $\boldsymbol{C}$ with and without wall depletion $\tilde{\boldsymbol{J}}_{\boldsymbol{r}}^{\boldsymbol{m,d\ p}}$ for eccentricity = at =

Figure 11 shows the radial distribution of C in the absence of flow, for eccentricities of $e = 0 - 3$. Brownian dynamics [24] simulation results for $e = 0$ [1] validate the continuum theory in the absence of flow, where $\tilde{}^{m,str}$ vanishes and only $\tilde{}_{r}^{m,dep}$ drives the polymer migration. Increasing eccentricity reduces the plateau due to the increased gap at $\theta = 0$. Increasing eccentricity also increases Gd. Note that $Gd = 0.$ is the highest we can achieve when wall-depletion is included, since a further increase of Gd would require an eccentricity beyond $e = 3.3$ which makes it impossible to maintain a mass balance in the narrow gap due to the depletion layer.

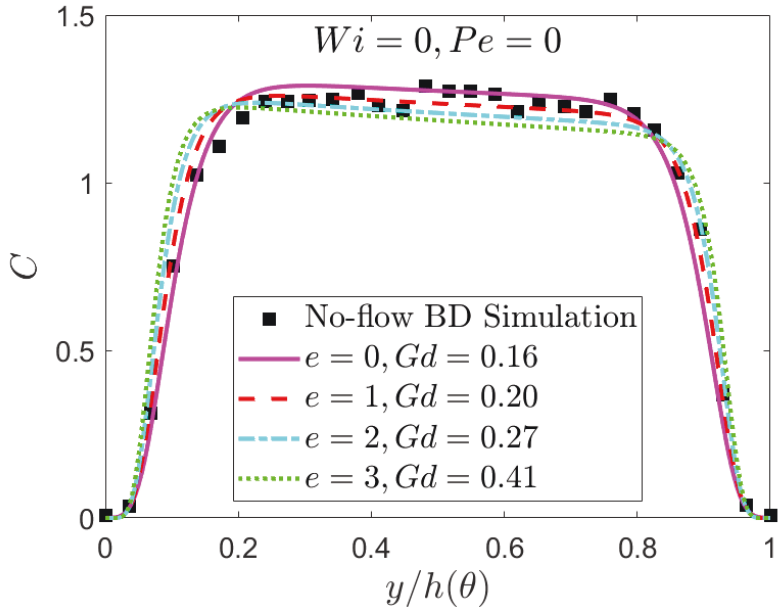

Figure 11 Radial distribution of $\boldsymbol{C}$ calculated by BD simulation for = and by constitutive theory for = ~**3** at = in the absence of flow

Figure 12 shows the radial distribution of C at different azimuthal angles for $e = 1$ in the presence of flow at $Wi = 0.4$. Similar migration patterns are observed at $\theta = 0, \frac{\pi}{2}, \pi, \frac{3\pi}{2}$, showing a depleted region near the wall. In the centre of the gap, a higher C is observed at $\theta = \pi$ than at $\theta = 0$, due to reduced gap at $\theta = \pi$ and mass balance.

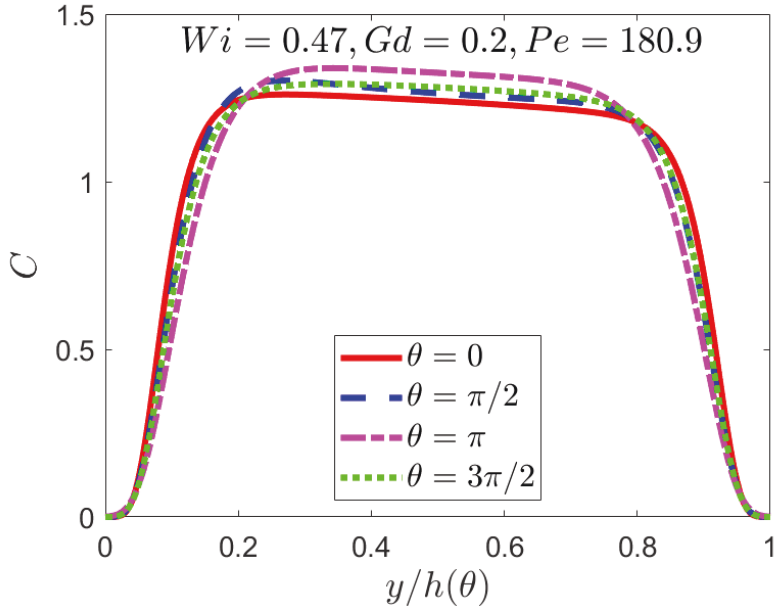

Figure 12 Radial distribution of $\boldsymbol{C}$ for eccentricity = at = $, \frac{\pi}{2}, \pi, \frac{3\pi}{2}$ in the presence of flow

Figure 13 shows the concentration distribution in the radial and circumferential directions for different Pe when both wall-depletion and stress-induced migration are present. No observable change of C in the radial direction is found when Pe changes from 0.08 to 180.9. However, the distribution of C in the circumferential direction is shifted downstream when $Pe > 1$, because of the influence of convection as also noticed in Figure 5. Note that Wi also increases from 2.0×10^{4} to 0.47. When Wi exceeds 1.6 the numerical solution of the continuum theory becomes unstable even when a minimum η=0.1 used, leaving the constitutive theory unreliable for higher Wi, regardless of the inclusion of wall-depletion as discussed for Figure **6** earlier. Continuum theory becomes unreliable in such circumstances and mesoscopic simulations such as Brownian dynamics [24] simulations will be required to track polymer dynamics and stress-gradient-induced migration.

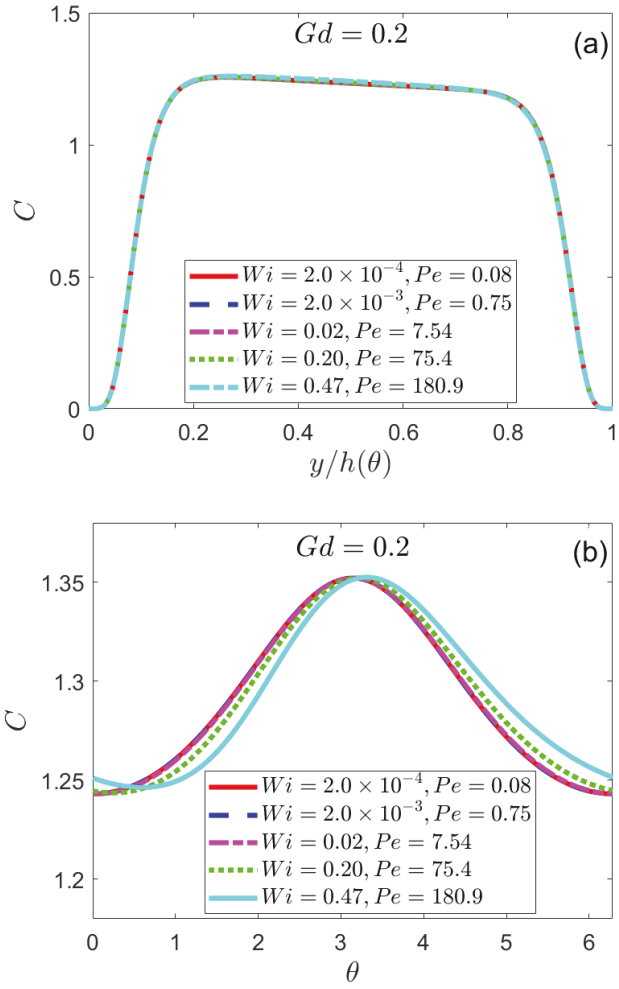

Figure 13 Distribution of $\boldsymbol{C}$ in the (a) radial direction at = and (b) circumferential direction at $\boldsymbol{y/h}$( ) = . for eccentricity = and for different values of $\boldsymbol{Wi}$

6. Conclusions

We have applied our recent continuum theory for the stress-gradient-induced migration of dilute polymer solutions to shearing flow between eccentric cylinders. A stress-gradient-induced migration drives polymers from the outer towards the inner cylinder for both concentric and eccentric cylinders. An increase of the rotation speed of the inner cylinder leads to an increase in both Weissenberg and Peclet numbers, Wi and Pe, which in turn increases the polymer concentration near the inner cylinder. The theory is valid at low values of the gradient number *Gd*, which is proportional to the ratio of the polymer radius of gyration to the gap. The migration forces given in Eqs. (10-14) are related to velocity and its derivatives, resulting in a dependence of polymer concentration on rotation speed V (and Wi, and Pe as they are proportional to V by definition). Predictions from the low order theory in Wi match well with those obtained from solving the full constitutive theory when Wi is small, i.e., when viscoelastic effects are small. But when Wi approaches 1, the perturbation theory fails, and stress must be obtained from the full constitutive theory which is valid up to arbitrarily high Wi. However, amplified numerical artefacts occur when using the constitutive theory (when $Wi > 1$) due to steep changes in the conformation tensor during calculation. An under-relaxation parameter is therefore used to stabilize the calculation for the constitutive theory i.e., $Wi > 1$. Nevertheless, a maximum of $Wi = 1.6$ is achieved with minimum under-relaxation η=0.1; the smaller η required to stabilize the calculation is computationally inefficient. For concentric cylinders, a much larger Wi (close to 4.71) can be applied, which shows the possibility of large migration effects in lubricated bearings with gaps comparable to the size of the polymer molecules [1]. In eccentric-cylinder flow, extensional components of the flow are generated, leading to an amplified deformation of the polymer molecules, at the same Weissenberg number Wi, although large migration effects are also possible for eccentric cylinders. In both concentric and eccentric cylinders, polymer migration is largely dictated by the coupled variations in the second derivatives of the velocity components. In the simplest case of concentric cylinders, these terms represent the effect of polymer alignment along curved streamlines, which drives polymer migration towards the centre of the streamline

curvature in the simplest case. This is analogous to surface tension along a curved surface, producing an inward migration towards the inner cylinder. It is the same driving force that produces rod climbing.

Wall-depletion-induced migration has a large effect on the polymer concentration profile, producing near-zero polymer concentrations near the cylinder walls and a nearly flat concentration plateau elsewhere, with a slight downward slope towards the outer wall. The coupling of the depletion layer to the velocity produces "depletion-stress-gradient-induced" migration, as the concentration gradient produced by depletion couples to the convection term, producing additional migration that is first order in Wi. In the presence of wall, beyond a maximum gradient number Gd of 0.5, the mass balance of polymer and stability of the system could not be maintained in the narrow gap region, presumably because the dumbbell size becomes comparable to that of the eccentric cylinder gap, which is further intensified by the depletion layer when Gd approaches 0.5. For a fixed gap, the Peclet number Pe is proportional to Wi and can reach a very large value for small Gd and modest Wi, leading to a downstream shift in the maximum polymer concentration. Gd, which is related to Wi and Pe as $Wi = \frac{1}{16}\, Gd^2\, Pe$, must be small regardless of whether Wi and Pe are small so that the velocity gradient varies only modestly across the polymer molecule. The required condition $Gd < 1$, implies that $Wi << Pe$. This work demonstrates the utility of the continuum theory for solving concentration profiles in eccentric cylinder flow even for large Pe, when Wi is smaller than 1.6 and when Gd is smaller than 0.5, with significant implications for use of polymer additives in lubricated bearings.

Supplementary Material

A complete list of migration terms and velocity components in cylindrical coordinates are available in Appendix I. Additional illustration of the numerical method used is also available in Appendix II.

Acknowledgement

This research was partially supported by the NSF under grants DMR 1403335 and DMR 1707640, and partially by a gift from Exxon-Mobil Research and Engineering. Any opinions, findings, and conclusions or recommendations expressed in this material are those of the authors and do not necessarily reflect the views of the National Science Foundation (NSF).

References

[1] Hajizadeh E and Larson R G 2017 Stress-gradient-induced polymer migration in Taylor–Couette flow *Soft Matter* **13** 5942-9

[2] MacDonald M J and Muller S J 1996 Experimental study of shear-induced migration of polymers in dilute solutions *Journal of Rheology* **40** 259-83

[3] Ru¨he J, Novotny V, Clarke T and Street G B 1996 Ultrathin Perfluoropolyether Films—Influence of Anchoring and Mobility of Polymers on the Tribological Properties *Journal of Tribology* **118** 663-8

[4] Apostolakis M V, Mavrantzas V G and Beris A N 2002 Stress gradient-induced migration effects in the Taylor–Couette flow of a dilute polymer solution *Journal of Non-Newtonian Fluid Mechanics* **102** 409-45

[5] Druetta P and Picchioni F 2019 Polymer and nanoparticles flooding as a new method for Enhanced Oil Recovery *Journal of Petroleum Science and Engineering* **177** 479-95

[6] Ma H and Graham M D 2005 Theory of shear-induced migration in dilute polymer solutions near solid boundaries *Physics of Fluids* **17** 083103

[7] Helfand E and Fredrickson G H 1989 Large fluctuations in polymer solutions under shear *Physical review letters* **62** 2468-71

[8] Mardis E R 2011 A decade's perspective on DNA sequencing technology *Nature* **470** 198-203

[9] Rezvantalab H, Zhu G and Larson R G 2016 The effect of wall depletion and hydrodynamic interactions on stress-gradient-induced polymer migration *Soft Matter* **12** 5883-97

[10] Sauer M, Angerer B, Ankenbauer W, Földes-Papp Z, Göbel F, Han K T, Rigler R, Schulz A, Wolfrum J and Zander C 2001 Single molecule DNA sequencing in submicrometer channels: state of the art and future prospects *Journal of biotechnology* **86** 181-201

[11] Chopra M and Larson R G 2002 Brownian dynamics simulations of isolated polymer molecules in shear flow near adsorbing and nonadsorbing surfaces *Journal of Rheology* **46** 831-62

[12] Tegenfeldt J O, Prinz C, Cao H, Huang R L, Austin R H, Chou S Y, Cox E C and Sturm J C 2004 Micro- and nanofluidics for DNA analysis *Analytical and bioanalytical chemistry* **378** 1678-92

[13] Bakajin O B, Duke T A J, Chou C F, Chan S S, Austin R H and Cox E C 1998 Electrohydrodynamic Stretching of DNA in Confined Environments *Physical review letters* **80** 2737-40

[14] Cannavacciuolo L, Winkler R G and Gompper G 2008 Mesoscale simulations of polymer dynamics in microchannel flows *EPL (Europhysics Letters)* **83** 34007

[15] Jin H, Kang K, Ahn K H and Dhont J K G 2014 Flow instability due to coupling of shear-gradients with concentration: non-uniform flow of (hard-sphere) glasses *Soft Matter* **10** 9470-85

[16] Jin H, Kang K, Ahn K H, Briels W J and Dhont J K G 2018 Non-local stresses in highly non-uniformly flowing suspensions: The shear-curvature viscosity *The Journal of Chemical Physics* **149** 014903
[17] Mavrantzas V G and Beris A N 1993 Modeling of the Rheology and Flow-Induced Concentration Changes in Polymer Solutions *Physical review letters* **70** 2659-
[18] Beris A N and Mavrantzas V G 1994 On the compatibility between various macroscopic formalisms for the concentration and flow of dilute polymer solutions *Journal of Rheology* **38** 1235-50
[19] Masao Doi and Onuki. A 1992 Dynamic coupling between stress and composition in polymer solutions and blends *Journal de Physique II, EDP Sciences* **2** 1631-56
[20] Milner S T 1991 Hydrodynamics of semidilute polymer solutions *Physical review letters* **66** 1477-80
[21] Mavrantzas V G and Beris A N 1992 Modeling of the rheology and flow-induced concentration changes in polymer solutions *Physical review letters* **69** 273-6
[22] Öttinger H C 1992 Incorporation of polymer diffusivity and migration into constitutive equations *Rheologica Acta* **31** 14-21
[23] Zhu G, Rezvantalab H, Hajizadeh E, Wang X and Larson R G 2016 Stress-gradient-induced polymer migration: Perturbation theory and comparisons to stochastic simulations *Journal of Rheology* **60** 327-43
[24] Ruzicka B, Zaccarelli E, Zulian L, Angelini R, Sztucki M, Moussaïd A, Narayanan T and Sciortino F 2011 Observation of empty liquids and equilibrium gels in a colloidal clay *Nature Materials* **10** 56-60
[25] Tichy J A 1996 Non-Newtonian Lubrication With the Convected Maxwell Model *Journal of Tribology* **118** 344-8
[26] Öttinger H C 1987 A model of dilute polymer solutions with hydrodynamic interaction and finite extensibility. I. Basic equations and series expansions *Journal of Non-Newtonian Fluid Mechanics* **26** 207-46
[27] Jiang W, Huang J, Wang Y and Laradji M 2007 Hydrodynamic interaction in polymer solutions simulated with dissipative particle dynamics *The Journal of Chemical Physics* **126** 044901
[28] Hajizadeh E, Todd B D and Daivis P J 2014 Shear rheology and structural properties of chemically identical dendrimer-linear polymer blends through molecular dynamics simulations *The Journal of Chemical Physics* **141** 194905
[29] Hajizadeh E, Todd B D and Daivis P J 2014 Nonequilibrium molecular dynamics simulation of dendrimers and hyperbranched polymer melts undergoing planar elongational flow *Journal of Rheology* **58** 281-305
[30] Hajizadeh E, Todd B D and Daivis P J 2015 A molecular dynamics investigation of the planar elongational rheology of chemically identical dendrimer-linear polymer blends *The Journal of Chemical Physics* **142** 174911
[31] Español P and Revenga M 2003 Smoothed dissipative particle dynamics *Physical Review E* **67** 026705
[32] Litvinov S, Ellero M, Hu X and Adams N A 2008 Smoothed dissipative particle dynamics model for polymer molecules in suspension *Physical Review E* **77** 066703
[33] Müller K, Fedosov D A and Gompper G 2015 Smoothed dissipative particle dynamics with angular momentum conservation *Journal of Computational Physics* **281** 301-15
[34] Jerrold E. Marsden and Thomas J. R. Hughes 1994 *Mathematical foundations on elasticity* (New York: Dover publications, INC)
[35] Rowlinson J S 1989 The Yukawa potential *Physica A: Statistical Mechanics and its Applications* **156** 15-34

[36] Larson R G 1988 *Constitutive Equations for Polymer Melts and Solutions* (Stoneham: Butterworth-Heinemann)
[37] Huang Q, Mednova O, Rasmussen H K, Alvarez N J, Skov A L, Almdal K and Hassager O 2013 Concentrated Polymer Solutions are Different from Melts: Role of Entanglement Molecular Weight *Macromolecules* **46** 5026-35
[38] Hajizadeh E 2015 Molecular dynamics simulation of planar extensional and shear rheology of dendritic and blended dendrimer-linear polymer melts. (Australia: Swinburne University of Technology, PhD Thesis)
[39] Ellero M and Español P 2018 Everything you always wanted to know about SDPD⋆ (⋆but were afraid to ask) *Applied Mathematics and Mechanics* **39** 103-24
[40] Jendrejack R M, Dimalanta E T, Schwartz D C, Graham M D and de Pablo J J 2003 DNA dynamics in a microchannel *Physical review letters* **91** 038102
[41] Jendrejack R M, Schwartz D C, Graham M D and de Pablo J J 2003 Effect of confinement on DNA dynamics in microfluidic devices *The Journal of Chemical Physics* **119** 1165-73